

Multiphase Signatures of AGN Feedback in Abell 2597

G. R. Tremblay,^{1,2,3} C. P. O’Dea,^{2,4} S. A. Baum,^{3,5} T. E. Clarke,⁶ C. L. Sarazin,⁷
J. N. Bregman,⁸ F. Combes,⁹ M. Donahue,¹⁰ A. C. Edge,¹¹ A. C. Fabian,¹² G. J. Ferland,¹³
B. R. McNamara,^{4,14} R. Mittal,³ J. B. R. Oonk¹⁵ A. C. Quillen,¹⁶ H. R. Russell,¹⁴
J. S. Sanders,¹² P. Salomé,⁹ G. M. Voit,¹⁰ R. J. Wilman,¹¹ and M. W. Wise¹⁵

¹ European Southern Observatory, Karl-Schwarzschild-Str. 2, 85748 Garching bei München, Germany; grant.tremblay@eso.org

² Department of Physics, Rochester Institute of Technology, 84 Lomb Memorial Drive, Rochester, NY 14623, USA

³ Chester F. Carlson Center for Imaging Science, 54 Lomb Memorial Drive, Rochester, NY 14623, USA

⁴ Harvard-Smithsonian Center for Astrophysics, 60 Garden St., Cambridge, MA 02138, USA

⁵ Radcliffe Institute for Advanced Study, 10 Garden St., Cambridge, MA 02138, USA

⁶ Naval Research Laboratory Remote Sensing Division, Code 7213 4555 Overlook Ave SW, Washington, DC 20375, USA

⁷ Department of Astronomy, University of Virginia, P.O. Box 400325, Charlottesville, VA 22904-4325, USA

⁸ University of Michigan, Department of Astronomy, Ann Arbor, MI 48109, USA

⁹ Observatoire de Paris, LERMA, CNRS, 61 Av. de l’Observatoire, 75014 Paris, France

¹⁰ Michigan State University, Physics and Astronomy Dept., East Lansing, MI 48824-2320, USA

¹¹ Department of Physics, Durham University, Durham, DH1 3LE, UK

¹² Institute of Astronomy, Madingley Rd., Cambridge, CB3 0HA, UK

¹³ Department of Physics, University of Kentucky, Lexington, KY 40506, USA

¹⁴ Physics & Astronomy Dept., Waterloo University, 200 University Ave. W., Waterloo, ON, N2L 2G1, Canada

¹⁵ ASTRON, Netherlands Institute for Radio Astronomy, P.O. Box 2, 7990 AA Dwingeloo, The Netherlands

¹⁶ Department of Physics and Astronomy, University of Rochester, Rochester, NY 14627, USA

Accepted for Publication in MNRAS, 9 May 2012

ABSTRACT

We present new *Chandra* X-ray observations of the brightest cluster galaxy (BCG) in the cool core cluster Abell 2597 ($z = 0.0821$). The data reveal an extensive kpc-scale X-ray cavity network as well as a 15 kpc filament of soft-excess gas exhibiting strong spatial correlation with archival VLA radio data. In addition to several possible scenarios, multiwavelength evidence may suggest that the filament is associated with multiphase ($10^3 - 10^7$ K) gas that has been entrained and dredged-up by the propagating radio source. Stemming from a full spectral analysis, we also present profiles and 2D spectral maps of modeled X-ray temperature, entropy, pressure, and metal abundance. The maps reveal an arc of hot gas which in projection borders the inner edge of a large X-ray cavity. Although limited by strong caveats, we suggest that the hot arc may be (a) due to a compressed rim of cold gas pushed outward by the radio bubble or (b) morphologically and energetically consistent with cavity-driven active galactic nucleus (AGN) heating models invoked to quench cooling flows, in which the enthalpy of a buoyant X-ray cavity is locally thermalized as ambient gas rushes to refill its wake. If confirmed, this would be the first observational evidence for this model.

Key words: galaxies: clusters: individual: Abell 2597 – galaxies: active – galaxies: star formation – galaxies: clusters: intracluster medium – galaxies: clusters: general

1 INTRODUCTION

Although an important component in models of galaxy evolution, little is known about the mechanical interaction between active galactic nucleus (AGN) outflows and the ambient gaseous environments through which they propagate. Observations of brightest cluster galaxies (BCGs) in cool core (CC) clusters suggest that the outflowing plasma can drive sound waves and subsonically excavate cavities in the ambient X-ray bright intracluster medium (ICM,

e.g., Sarazin 1986), acting as lower-limit calorimeters to the AGN kinetic energy input (Böhringer et al. 1993; Fabian et al. 2000, 2006; Churazov et al. 2001; McNamara et al. 2000, 2001; Blanton et al. 2001; Nulsen et al. 2005; Forman et al. 2005, 2007; Bîrzan et al. 2004). Along with a wealth of supporting circumstantial evidence, these observations motivate the radio-mode AGN feedback paradigm, invoked at late epochs to inhibit catastrophic cooling flows that should otherwise drive extreme star formation rates in

the BCG (e.g., reviews by Fabian 1994; Peterson & Fabian 2006; McNamara & Nulsen 2007, 2012; Fabian 2012). However, while the cavities demonstrate the profound impact of jets on ambient hot X-ray haloes, the physics coupling AGN mechanical energy to ICM structure and entropy remain poorly understood.

Moreover, models invoking radio-mode feedback to quench cooling flow signatures such as star formation must be reconciled with observational evidence that, in several systems, the propagating radio source triggers rather than inhibits star formation. *Hubble Space Telescope (HST)* FUV observations of several CC BCGs reveal knots of young stars preferentially aligned along the edges of radio lobes — sites where the outflowing plasma collides with the observed ambient cold gas (e.g., Abell 1795, Abell 2597, O’Dea et al. 2004; Tremblay et al. 2012b, and references therein). Many studies have suggested that the jet propagation front can shock and compress these cold clouds, inducing rapid, short-duration starbursts (e.g., Elmegreen & Elmegreen 1978; Voit 1988; De Young 1989; McNamara & O’Connell 1993; O’Dea et al. 2004; Batchelder et al. 2007; Holt et al. 2008, 2011). Mass loading of the jet can similarly induce deceleration and bending of the radio source in regions of high gas density, which could explain the compact, steep spectrum, and bent Fanaroff & Riley (1974) class I (FR I) morphologies commonly associated with radio sources embedded in dense environments (e.g., O’Dea & Baum 1986; Baum et al. 1988).

Progress in understanding these issues rests on a better grasp of the complex ways in which AGN outflows interact not only with their hot gaseous environments, but with the colder ISM phases as well. In this paper we present new *Chandra X-ray Observatory* observations, totaling 150 ksec in combined effective exposure time, of the brightest cluster galaxy (BCG) at the centre of the cool core cluster Abell 2597 ($z = 0.0821$). Previous works have shown that the source exhibits extensive, multiphase ($10^3 - 10^7$ K) signatures of AGN/ISM interactions, including X-ray cavities, evidence for gas entrainment, and jet-triggered star formation (e.g., Sarazin et al. 1995; Taylor et al. 1999; O’Dea et al. 2004; Clarke et al. 2005; Oonk et al. 2010). In Section 2 we describe the observations, data reduction, and our procedure for the creation of 2D spectral maps from the new X-ray data. In Section 3 we present spatial and spectral results, including general X-ray morphology, radio/X-ray spatial correlations, surface brightness and spectral parameter radial profiles, and a hardness analysis. In Section 4 we present the 2D spectral maps of modeled X-ray gas properties including temperature, entropy, pressure, and metal abundance. In Sections 5 and 6 we discuss the main results of this paper, namely the “cold filament” and “hot arc” features (respectively). Throughout this work, we adopt $H_0 = 71 h_{71}^{-1} \text{ km s}^{-1} \text{ Mpc}^{-1}$, $\Omega_M = 0.27$, and $\Omega_\Lambda = 0.73$. In this cosmology, $1''$ corresponds to ~ 1.5 kpc at the redshift of the A2597 BCG ($z = 0.0821$). This redshift corresponds to an angular size distance of $D_A \approx 315$ Mpc and a luminosity distance of $D_L \approx 369$ Mpc. A discussion of these new X-ray observations in the context of ICM cooling and AGN heating can be found in a companion paper (Tremblay et al. 2012b).

2 OBSERVATIONS & DATA REDUCTION

A summary of all new and archival data used (directly or referentially) in this analysis can be found in Table 1 of Tremblay et al. (2012b). Here we describe the two new *Chandra X-ray Observatory* AXAF CCD Imaging Spectrometer (ACIS) exposures of the A2597 BCG, taken in May 2006 for a total of 52.8 and 60.9 ksec,

respectively (ObsIDs 6934 and 7329, PI: Clarke). Both observations were taken in VFaint, full-frame, timed exposure mode. An older 40 ksec *Chandra* exposure (ObsID 922, PI: McNamara) was taken in July 2000 and originally published by McNamara et al. (2001) (hereafter M01) in a study of the A2597 ghost cavity (which we will discuss later). This observation was taken in Faint, full-frame, timed exposure mode. As noted in M01, ObsID 922 was badly impacted by flaring events, yielding only ~ 18 ksec of data suitable for spectral analysis. We have re-processed all of these observations in a uniform manner, as described below.

The three observations (ObsIDs 922, 6934, and 7329) were obtained as primary data products from the *Chandra* Data Archive. The data were reduced in version 4.2 of the CIAO environment (*Chandra* Interactive Analysis of Observations, Fruscione et al. 2006) using version 4.3.1 of the calibration database (CALDB). The CIAO script `chandra_repro` was run for each observation to automate the creation of new `level=1` and `level=2` event files by applying charge transfer inefficiency (CTI) correction, time-dependent gain adjustment, PHA and pixel randomization, and standard grade and status filtering. Only those events with ASCA grades 0, 2, 3, 4, and 6 are used in this analysis. Background light curves for each exposure were obtained from the ACIS-S1 back-illuminated chip. The CIAO script `deflare` was used to create good time interval (GTI) temporal masks rejecting counts associated with three sigma flares over the mean quiescent background rate. This filtering strategy retained only ~ 18 (out of 40) ksec of flare-free data for the 922 observation. ObsIDs 6934 and 7329 were not significantly impacted by flaring events, and no more than 2 ksec for either observation were rejected. The combined effective exposure time is 150 ksec, and the combined flare-free exposure time is 128 ksec.

A 0.5-7 keV energy filter was applied to the reduced exposures using standard `dmcopy` techniques. The `fluximage` script was then used to create exposure maps for each dataset. The observations were reprojected to a common WCS tangent point, combined, and divided by their similarly reprojected and combined exposure maps, creating exposure-corrected 0.5-7 keV mosaics suitable for spatial analysis. Soft (0.5-1 keV), medium (1-2 keV), and hard (2-7 keV) combined images were also created using this strategy. Adaptively smoothed and unsharp mask images were made using techniques discussed in Section 3. Merged data are not suitable for spectral analysis, so X-ray spectra were extracted from each individual observation and analyzed simultaneously in XSPEC version 12.5 (Arnaud 1996). We have also created 2D spatial+spectral maps of projected X-ray temperature, pressure, and metal abundance, following a procedure described below.

2.1 Creation of X-ray spectral maps

Using the spatially resolved *Chandra* spectroscopy, we have created 2D maps of projected X-ray temperature, pseudo-entropy, pseudo-pressure, and metal abundance. We briefly describe how these maps were created below, but refer the reader to Section 3 for more details on (e.g.) how spectra are extracted and modeled.

To make the spectral maps, the exposure corrected mosaic was cleaned of contaminating point sources, cropped to include only the inner $80'' \times 80''$ (120×120 kpc), then passed through the `CONTBIN`¹ adaptive binning algorithm described by Sanders

¹ <http://www-xray.ast.cam.ac.uk/papers/contbin/>

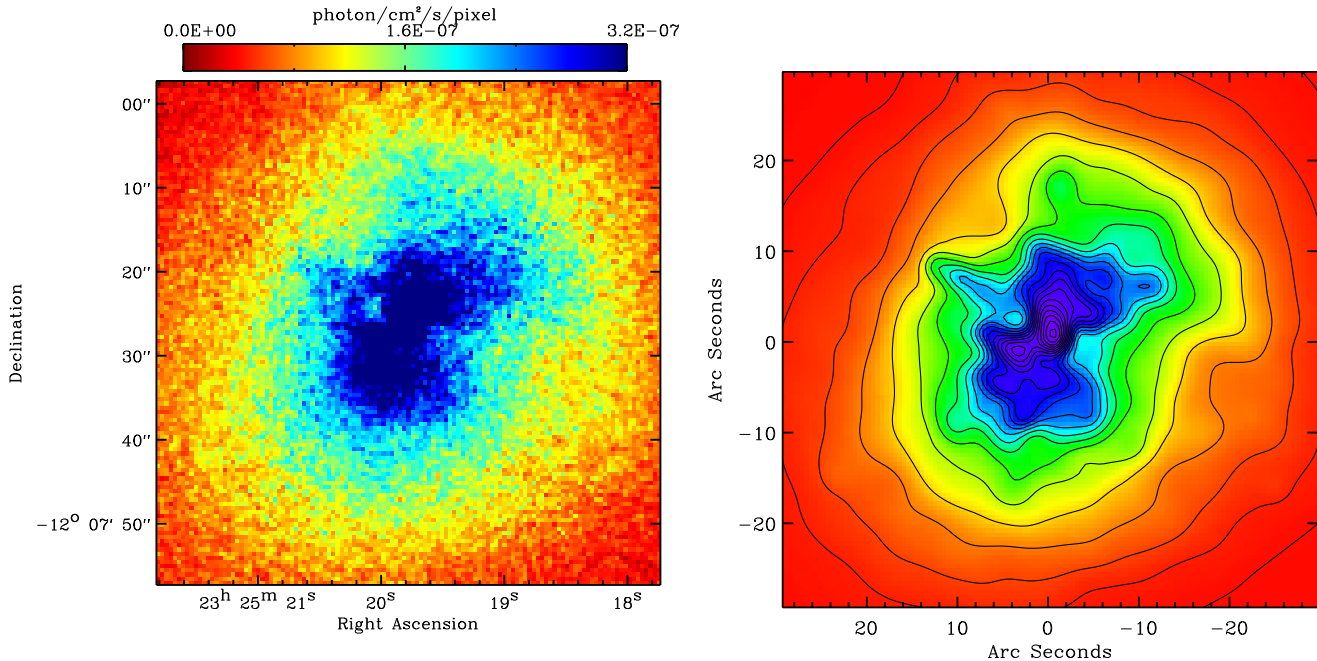


Figure 1. (left) Exposure corrected (fluxed) 0.5-7 keV image of the three merged *Chandra* exposures 922, 6934, and 7329. No gaussian smoothing or pixel binning has been applied. (right) 0.5-7 keV X-ray surface brightness map, smoothed with an adaptive gaussian kernel. Black contours have been overlaid to better show the spatially anisotropic nature of the emission. The innermost contour marks a flux of 4.6×10^{-7} photons $\text{sec}^{-1} \text{cm}^{-2} \text{pixel}^{-1}$, and the contours move outward with a flux decrement of 2.0×10^{-8} photons $\text{sec}^{-1} \text{cm}^{-2} \text{pixel}^{-1}$. Both panels share an identical field of view, centered at RA=23h 25m 19.75s, Dec = -12° 07' 26.9'' (J2000).

(2006). The code locates the brightest pixel in the image and creates a spatial bin around it by including all neighboring pixels of like surface brightness until a user-defined signal-to-noise threshold is met, and iteratively moves outward following the same procedure. For the X-ray temperature and emission measure maps (used in the pseudo-entropy and pressure maps), we set this threshold to be $S/N=30$, or $\gtrsim 30^2 = 900$ counts. For the metal abundance map, we set it to $S/N=70$. The shape of each spatial bin was constrained so that its length could be at most two times its width (to prevent “stripe”-like bins which would sample an unreasonably large spatial cross section of multiphase cluster gas). The result is a spatially binned image that follows the surface brightness distribution. In addition to the contour binned image, the algorithm creates a bin map which we used with J. Sanders’ `make_region_files` code to create CIAO-compatible region files for each of the 277 individual spatial bins created for our data by the `CONTBIN` code. The individual `level=2` event files for *Chandra* ObsIDs 6934 and 7329 (which were similarly cleaned of point sources) were then spatially reprojected to identical positions using the merged image as a coordinate reference. The region files created from the bin map were then ported to each of the two event files. A script was used to iteratively extract the source spectrum, background file, and create associated response files (ARF/RMF) for each of the 277 spatial regions on each of the two event files. The corresponding source and background spectra from like regions on the two exposures were then added together using the `mathpha` tool in CIAO, and average responses were created using `addarf` and `addrmf` from `FTOOLS`. The summed spectra were then regrouped to 15 count bins, and the `BACKSCAL` and `EXPOSURE` header keywords were updated. This procedure is only viable if the exposures were taken on the same

chip (which is true for ObsIDs 6934 and 7329). The 18 ksec (good time) 922 dataset was therefore not used in this part of the analysis.

An XSPEC v12.5 (Arnaud 1996) TCL script was used to fit Mewe-Kaastra-Liedahl thermal plasma models (called `MEKAL` in XSPEC), absorbed to account for Galactic attenuation (i.e., `WABS × MEKAL`). These models were fit simultaneously to the two grouped, background-subtracted spectra extracted from each of the matched regions of the two exposures. For each fit, the source redshift was fixed to $z = 0.0821$, the hydrogen column density N_{H} was frozen to the Galactic value of $2.48 \times 10^{20} \text{ cm}^{-2}$ (McNamara et al. 2001), and the gas temperature kT , abundance Z , and normalization N_{MEK} (effectively the emission measure) were allowed to vary. The fits were run iteratively to minimize the χ^2 statistic. The best-fit parameters kT , Z , N_{MEK} , and their corresponding upper and lower 90% confidence intervals were written to individual files linked to their corresponding spatial bin. J. Sanders’ script `paint_output_images` was then used to rescale the spatial bins in the `CONTBIN` output image by their associated best-fit parameters, producing projected temperature, emission measure, and abundance maps. A projected pseudo-pressure map was then created by multiplying the square root of the emission measure map (which is proportional to but not exactly the density, which requires an uncertain volume assumption) by the temperature (kT) map. The maps were then adaptively smoothed using the same variable-width Gaussian kernel sizes used for the smoothed surface brightness map shown in Fig. 1b.

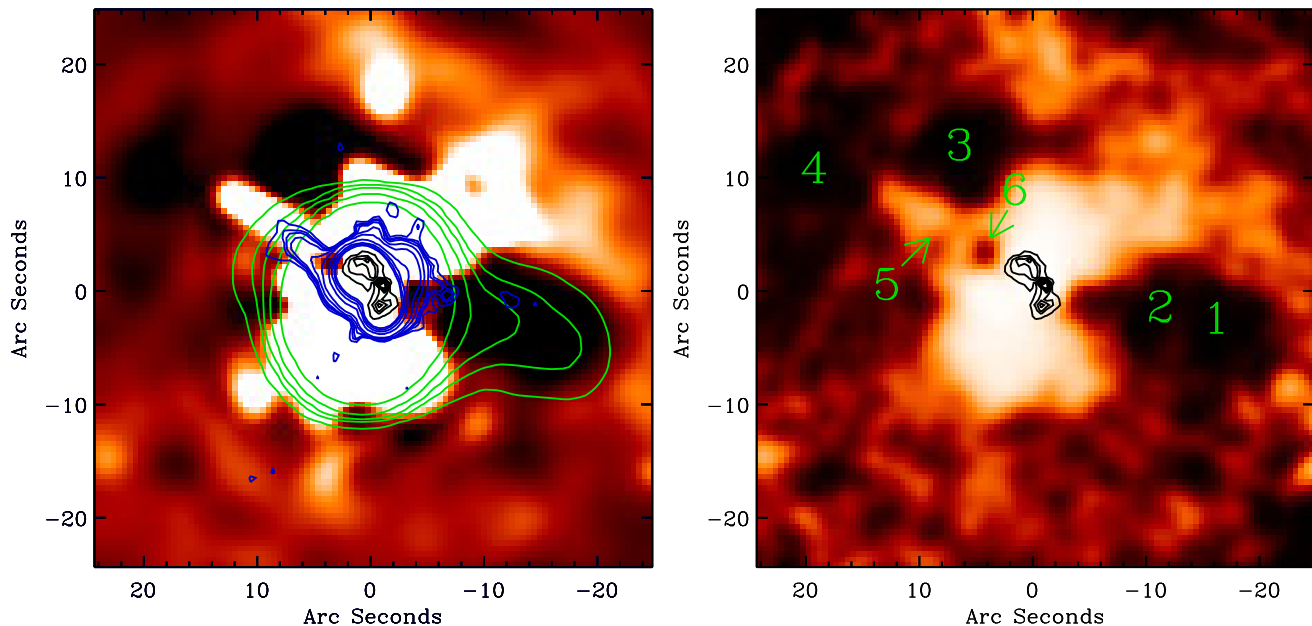


Figure 2. Two unsharp mask images of the merged 150 ksec *Chandra* 0.5-7 keV observation. The panel at *left* was made via subtraction of a $20''$ Gaussian smoothed version of the image from the adaptively smoothed version. The version in the *right* panel was made by subtracting the same $20''$ Gaussian smoothed version of the image from a $5''$ Gaussian smoothed version, then dividing by the sum of the two images. In the chosen color scheme, regions of X-ray surface brightness excess over the subtracted smoothed counts appear in red/orange, while deficits appear in black. 330 MHz VLA contours from have been overlaid in green, while the 1.3 GHz radio contours are plotted in blue, and the 8.4 GHz radio contours appear in black. All of the radio data is from Clarke et al. (2005). Note how the extended 330 MHz emission corresponds in both linear extent and projected P.A. with the apparent X-ray cavity consisting of features (1) and (2), as labeled in the right panel. Note also that the northeast hook of the 1.3 GHz emission (blue) is aligned with the “bottom” of the 15 kpc X-ray filament. The major morphological features which will be the subject of further spatial and spectral analysis have been labeled 1-6 in the right panel. Although we label them separately, we do not mean to imply that features 1 and 2 are necessarily discrete. Rather, feature 1 is labeled separately to enable a clearer comparison with the McNamara et al. (2001) “ghost cavity”. Features 1 and 2 may well be one larger cavity. The ring features seen in the left-hand panel are artifacts from subtracting images with different smoothing lengths.

3 X-RAY SPATIAL AND SPECTRAL RESULTS

3.1 General X-ray morphology

Previous X-ray studies have been published for A2597 using the 40 ksec (18 ksec of good time) *Chandra* observation 922 (e.g., M01 and Clarke et al. 2005, hereafter C05). M01 was the first to report on the western and northeastern ghost cavities inferred from localized depressions in the X-ray surface brightness. Later work by C05 extended this analysis to include a study between X-ray morphology and Very Large Array (VLA) radio observations at 8.4 GHz, 1.3 GHz, and 330 MHz. That work described an X-ray “tunnel” apparent in their unsharp mask of the 922 data. Roughly $22''$ (33 kpc) in projected length and $1''.5$ (2.3 kpc) in projected radius, the tunnel appeared to connect the peak of the X-ray surface brightness distribution, cospatial with the radio and BCG optical core, with the M01 western cavity. It was not apparent whether this was a discrete feature, or was part of a larger cavity encompassing both the tunnel and the M01 cavity. Extended 330 MHz radio emission was observed to be cospatial with both features.

In Fig. 1 we present the new, combined 0.5-7 keV data. The left panel shows the exposure corrected mosaic with no spatial binning or smoothing applied. The right panel shows the merged data adaptively smoothed with a variable width gaussian kernel whose size self-adjusts to match the local event density. Black surface brightness contours are overlaid to make individual features eas-

ier to view. The innermost contour marks a flux of 4.6×10^{-7} photons $\text{sec}^{-1} \text{cm}^{-2} \text{pixel}^{-1}$, and move outward with a decrement of 2.0×10^{-8} photons $\text{sec}^{-1} \text{cm}^{-2} \text{pixel}^{-1}$. Both panels share the same scale, with a field of view (FOV) of $\sim 60'' \times 60''$, corresponding to $90 \text{ kpc} \times 90 \text{ kpc}$. The FOV is centered on the X-ray centroid at RA=23h 25m 19.75s, Dec = $-12^\circ 07' 26.9''$ (J2000). As with all figures presented in this paper, North is up, and East is left.

The X-ray surface brightness distribution is highly anisotropic, and extended along a position angle that matches the major axis of the BCG stellar isophotes (which lie on a P.A. $\sim -45^\circ$, where North through East, or counter-clockwise, is the positive direction). The spatial anisotropy of the X-ray emission seems to be confined to the scale of the BCG, as the X-ray isophotes assume a smoother elliptical shape in the outermost regions.

As seen in Fig. 1, the innermost $20''$ of the 0.5-7 keV emission is distributed in a butterfly-like shape, with two high surface brightness knots $\sim 1''$ W and $\sim 3''$ SE of the X-ray centroid. The knot $1''$ W is approximately cospatial with the radio core. A fraction of the X-ray emission in this knot stems from the weak point source associated with the AGN. Two sharp deficits of X-ray emission $\sim 2''$ NE and $\sim 2''$ SW define the inner ridges of the “butterfly wings”. One of the most prominent features visible in Fig. 1 is a $10''$ (~ 15 kpc in projection) filament extending along a P.A. $\approx 55^\circ$, roughly perpendicular to the major axis of the butterfly feature and aligned (in projection) along the minor axis of the BCG stellar isophotes.

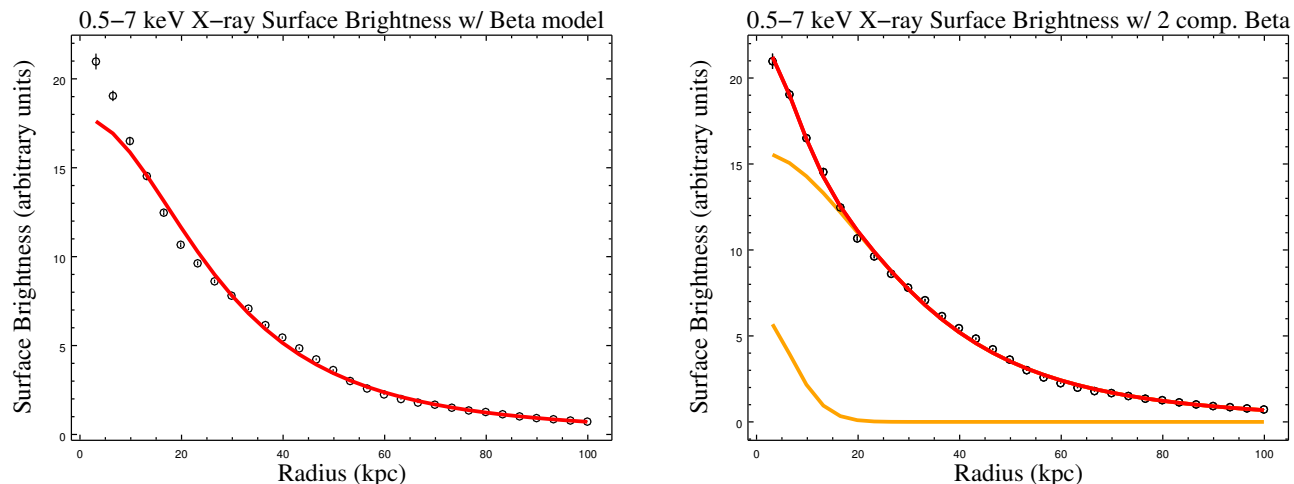


Figure 3. X-ray surface brightness profiles extracted from a series of concentric annuli spanning from the central regions out to 100 kpc. (*left*) A one component beta model has been fit. (*right*) A two-component (additive) beta model has been fit, yielding better overall correspondence to the measured profile. The additive two-component model is in red, while the two individual components to the model are shown in orange.

The western edge of the M01 ghost cavity is faintly seen $\sim 18''$ W, $5''$ S of the centre.

In Fig. 2 we show the same 0.5-7 keV data processed in two ways: (1) a residual image made by subtracting a $30''$ gaussian smoothed image from the adaptively smoothed image shown in Fig. 1b, and (2) a more conventional unsharp mask made by subtracting a $20''$ gaussian smoothed image from a $5''$ (non-adaptive) gaussian smoothed version. The subtracted data is then divided by the sum of the two images. Regions of X-ray surface brightness excess over the subtracted smooth background appear in white, while deficits (cavities) appear in black. Both panels are on the same scale, with identical $50'' \times 50''$ ($75 \text{ kpc} \times 75 \text{ kpc}$) FOVs. We overlay radio contours on the left panel, which we will discuss later. These two edge enhancement methods (particularly method 1) are inherently noisy, and introduce artifacts that complicate quantitative morphological analysis. Significance of the observed features must therefore be estimated from the un-processed data. We show these mostly as viewing aids for the major morphological features.

By comparing unsmoothed counts in like sized regions at the same cluster-centric radius, we find six discrete features associated with $\gtrsim 10\sigma$ deficits or excesses relative to the local mean. These features are labeled 1-6 in the right panel of Fig. 2. This paper discusses feature (5), the ‘‘cold filament’’, while energetics analysis of the X-ray cavities is discussed in a companion paper on AGN heating and ICM cooling in A2597 (Tremblay et al. 2012b).

3.2 Radio & X-ray spatial correlations

In Fig. 2a we overlay 8.4 GHz, 1.3 GHz, and 330 MHz VLA radio contours in black, blue, and green (respectively). We do not show the innermost 1.3 GHz and 330 MHz contours to allow the higher frequency contours to be clearly visible. As noted by M01 and C05, the northern and southern lobes of the 8.4 GHz source (black contours) are bounded to the west and east by deficits of X-ray emission associated with features (6) and (2), respectively. Beyond this, it is difficult to discern whether or not the 8.4 GHz lobes are interacting with the keV gas on these scales. No X-ray cavities are

observed to be directly cospatial with the 8.4 GHz lobes, though this lack of evidence should not be interpreted as evidence of absence. Any cavities that may exist on these scales would be very difficult to detect given a combination of (a) the compactness of the radio source compared to the X-ray emission and (b) a great deal of intervening keV gas along the line of sight. We expect that any cavities associated with the 8.4 GHz lobes would be associated with surface brightness decrements of a few percent at most, strongly limiting their detectability. Past literature presents strong evidence (e.g., Koekemoer et al. 1999; O’Dea et al. 2004) that the 8.4 GHz source is dynamically interacting with the $\sim 10^4$ K emission line nebula, which we will discuss later.

The 330 MHz VLA A-configuration observation (in green contours) does not resolve structures at the scale of the 8.4 GHz source, though a prominent arm of emission extends ~ 70 kpc to the west (projected) in strong spatial correlation with the western large cavity (feature 1+2). It is worth noting that the symmetric 50 pc scale jets in the VLBA map of Taylor et al. (1999) are approximately aligned (within $\sim 5^\circ$) with the major axis of the western large cavity and the extended 330 MHz emission (though this of course involves a comparison at vastly different scales). The blue 1.3 GHz contours are extended along the same axis as the 330 MHz eastern extension, the projected VLBA jet axis, the western large cavity, as well as ~ 8 kpc along the bottom half of the 15 kpc X-ray filament (feature 5). The NE 1.3 GHz hook, which is ~ 15 kpc from the radio core, also covers the C05 filament base cavity, (feature 6). There is also a ~ 1 kpc extension to the SW, into the bottom opening of the western large cavity.

The projected spatial coincidence of all of these features is strong evidence for a common, current jet axis. While the P.A. of the 8.4 GHz source is offset from this axis, it is the exception, and may arise from dynamical frustration of the jet as it propagates amid the dense molecular medium harboring the emission line nebula (this has been discussed by e.g., Sarazin et al. 1995; Koekemoer et al. 1999; O’Dea et al. 2004; Oonk et al. 2010). The 1.3 GHz emission extended along the bottom half of the 15 kpc X-ray filament (feature 5 in Fig. 2) may be evidence for dredge-up of

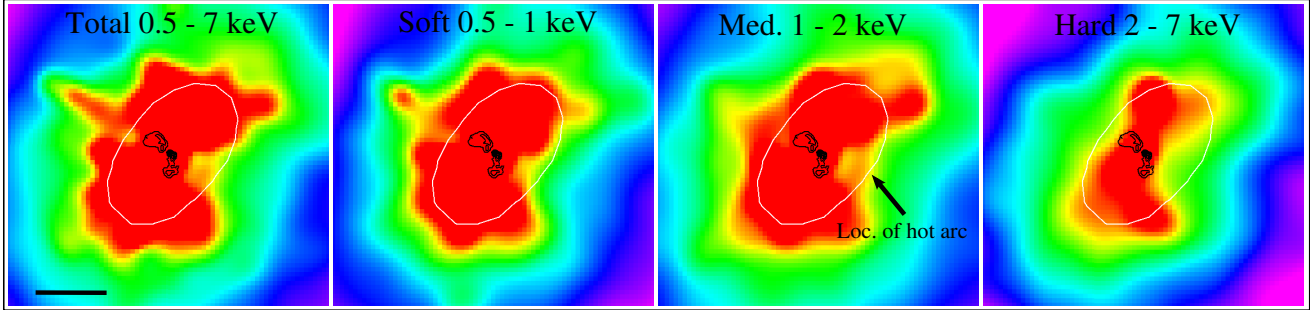


Figure 4. The adaptively smoothed *Chandra* image of A2597 shown at various slices in energy space, including (from left to right) “total” (0.5–7 keV), “soft” (0.5–1 keV), “medium” (1–2 keV), and “hard” (2–10 keV) emission. In black contours, we overlay the 8.4 GHz radio contours of PKS 2322-122, and in white contours we overlay a stellar isocontour from the *HST* R-band observation of the host galaxy. The black line at the bottom left corner of the leftmost panel marks a distance of $10''$ (15 kpc). Note that the major axis of the host galaxy stellar isophote is aligned along the same position angle as the X-ray major axis. The bright filament which extends 15 kpc NE from the center in the total and soft panels is effectively absent in the rightmost hard panel. The filament is therefore a soft excess, colder than the surrounding gas. The hard X-ray “disk” evident in the rightmost panel is aligned in projection with the isophotal major axis of its host galaxy’s stellar component.

lower temperature, high density keV gas by the propagating radio jet. Oonk et al. (2010) reported high velocity (and velocity dispersion) streams of H_2 and H II coincident with the southern edge of the northern 8.4 GHz radio lobe and approximately aligned with the projected VLBA jet axis. The jet may therefore be dynamically interacting with both the hot and warm/cold phases of the ISM. We will investigate these possibilities in Section 5.

3.3 X-ray Surface brightness Profile

In Fig. 3 we plot azimuthally summed X-ray surface brightness against projected radius, using fluxes extracted from narrow concentric annuli spanning $\sim 5 - 100$ kpc. We fit both singular and additive two-component Lorentz 1-D “beta” models with a varying power law (`beta1d` in CIAO Sherpa) to the data, wherein the surface brightness Σ_X at projected radius r varies as

$$\Sigma_X(r) = \Sigma_X(0) \left[1 + \left(\frac{r}{r_0} \right)^2 \right]^{(-3\beta+1/2)}. \quad (1)$$

Here, $\Sigma_X(0)$ is the central X-ray surface brightness and r_0 is the core radius. Typically, the ICM in galaxy clusters is well-fit by models with $\beta \approx 0.6$ (Sarazin 1986). Our results are consistent with this: if we fit a one-component beta model, shown in the left panel of Fig. 3, we find $\beta = 0.633$ with core radius $r_0 = 16.''4$ (or ~ 24 kpc). A far better fit is obtained with an additive two-component beta model, which we plot in the right panel in Fig. 3 (red line). This model consists of a $\beta = 0.686$ fit with a core radius of $r_0 = 19.''1$ (or ~ 29 kpc) and an inner steep component ($\beta = 10$) to fit the cusp (yellow lines). The small deviations between the model and data arise (in part) because the annuli from which the spectra are extracted effectively give an azimuthal average of X-ray fluxes that vary strongly as a function of position angle, owing to the morphologically disturbed nature of the X-ray gas. In the plots, error bars are shown, though difficult to see because they are generally smaller than the data points.

3.4 0.5–7 keV spectrum from a central 100 kpc aperture

We extract a spectrum from the individual flare-filtered ObsIDs 6934 and 7329, using a single circular aperture with a $63.''3$ (100 kpc) radius encompassing most of the sharply peaked central X-ray emission. Prior to this, we removed contaminating point

sources. The spectra were extracted using the CIAO 4.2 script `specextract`, and count-weighted response matrices were generated for each extraction.

Using simultaneous fitting techniques in XSPEC, we fit a variety of models to the total 0.5–7 keV spectrum extracted from the 100 kpc aperture. The most simple of these is a MEKAL model that has been absorbed to account for attenuation by the galactic hydrogen column (`WABS × MEKAL`). We also fit absorbed two-component MEKAL models (`WABS × [MEKAL + MEKAL]`) as well as the standard cooling flow model in XSPEC (`WABS × MKCFLOW`). Finally, we fit a “reduced” cooling flow model `WABS × [MEKAL + MKCFLOW]` (e.g., Rafferty et al. 2006), in which the high temperature MKCFLOW parameter is tied to the MEKAL kT parameter. The physical motivation behind this model is that AGN heating maintains the bulk of the gas at the ambient temperature (fit by the MEKAL component), while the MKCFLOW component models residual cooling from that ambient temperature (hence the parameter sharing below 0.1 keV (to which kT_{low} is fixed). In all cases, the source redshift was fixed to $z = 0.0821$.

Results from our modeling are shown in Table 1. As evident in column (8) of that table, the fits are uniformly “good” in terms of reduced χ^2 , indicative of the degeneracy that almost always arises from this type of X-ray spectral fitting. The last line of this table lists results from fitting the “reduced” cooling flow model, `WABS × [MEKAL + MKCFLOW]`, which has been used frequently in recent literature (e.g., Russell et al. 2010). We show this fit in Fig. 5 (green line). The individual additive model components (MEKAL and MKCFLOW) are shown in red solid lines and labeled accordingly. The high temperature parameter in the MKCFLOW component has been tied to the MEKAL ambient temperature component to simulate a residual cooling flow proceeding at low levels from the hot X-ray atmosphere. Fit residuals are shown in the bottom panel using the same color coding. They reach an $\sim 8\%$ maximum at the Fe L 1 keV peak. We discuss the residual cooling flow model for A2597 at greater length in Tremblay et al. (2012b).

3.5 Hardness analysis

In Fig. 4 we show soft (0.5–1 keV) through hard (2–7 keV) cuts in energy space for the adaptively smoothed combined *Chandra* data. In each panel we overlay the 8.4 GHz radio map in black contours, which for reference is ~ 10 kpc from end-to-end. The

WABS(MEKAL+MKCFLOW) Simultaneous Single 100 kpc Aperture Fit

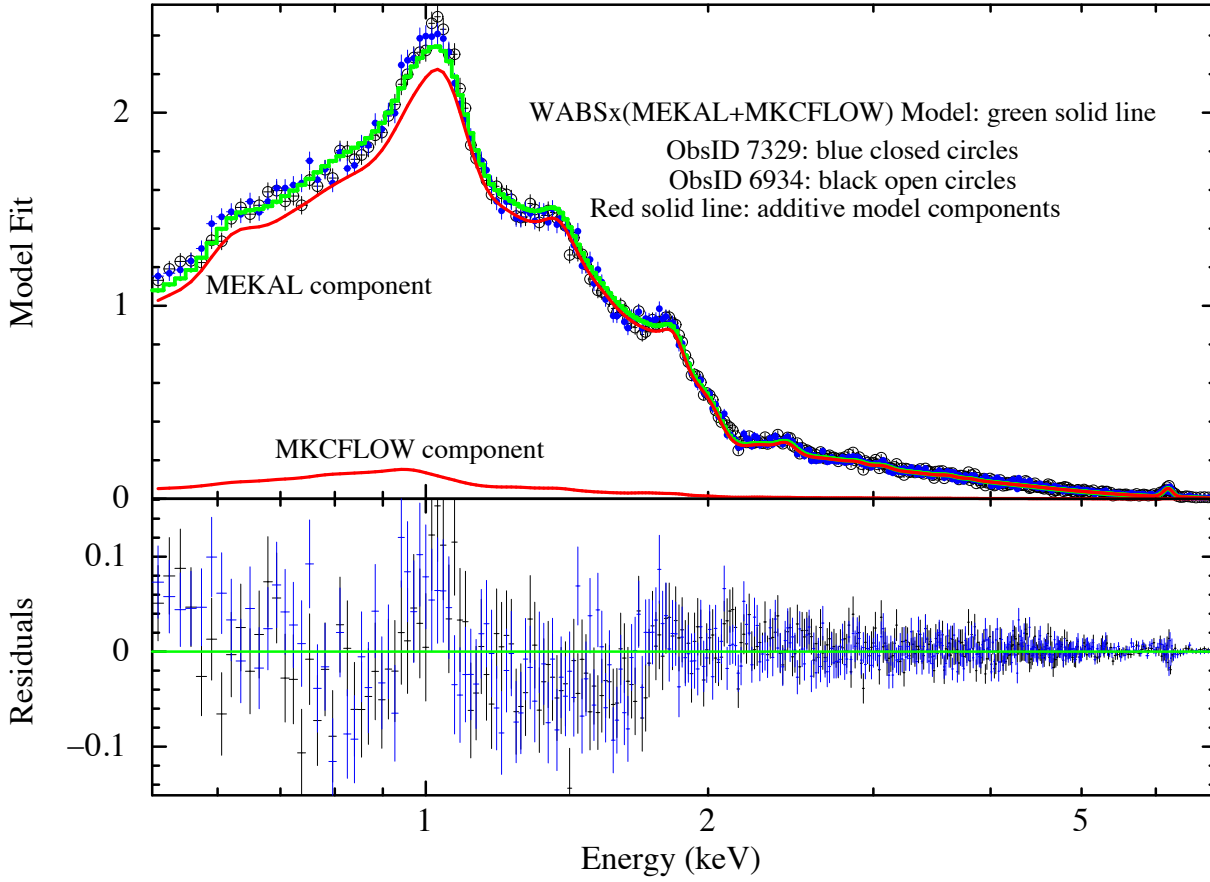


Figure 5. 0.5-7 keV X-ray spectrum of the innermost 100 kpc of the Abell 2597 BCG, extracted from *Chandra* observations 6394 (black open circles) and 7329 (blue closed circles). The spectra have extracted independently, grouped using a 30 count bin size, background subtracted, and fit simultaneously after removal of contaminating sources. A reduced cooling flow model (green solid line) has been fit to the data ($\text{WABS} \times [\text{MEKAL} + \text{MKCFLOW}]$ in XSPEC). The individual additive model components (MEKAL and MKCFLOW) are shown in red solid lines and labeled accordingly. The high temperature parameter in the MKCFLOW component has been tied to the MEKAL ambient temperature component to simulate a residual cooling flow proceeding at low levels from the hot X-ray atmosphere. Fit residuals are shown in the bottom panel using the same color coding. They reach an $\sim 8\%$ maximum at the Fe L 1 keV peak. Both panels are in units of normalized counts $\text{s}^{-1} \text{keV}^{-1}$. See the last entry in Table 1 for model parameters associated with this fit. Note that other model fits presented in the same table yield similar results in terms of reduced chi squared, illustrative of the degeneracy inherent in this sort of X-ray spectral fitting.

Table 1. Simultaneous spectral fits to the 0.5-7 keV X-ray spectrum extracted from a central 100 kpc aperture. Prior to extraction, a temporal filter was applied to the data to reject flaring events, and compact sources associated with other cluster members as well as the central weak point source associated with the AGN was removed. The spectra were rebinned using a 30 count threshold. Observation 922 has been excluded from spectral analysis due to significant flaring events and high background levels. Symmetric one sigma confidence intervals are shown on fit parameters. Parameters that have been frozen to a specific value prior to fitting are shown in parentheses. In the last model, $\text{WABS} \times [\text{MEKAL} + \text{MKCFLOW}]$, we tie the high temperature MKCFLOW parameter to the MEKAL kT parameter, following similar “reduced” cooling flow modeling in the literature (e.g., Rafferty et al. 2006; Russell et al. 2010).

XSPEC Model (1)	N_{H} ($\times 10^{20} \text{ cm}^{-2}$) (2)	kT_{low} (keV) (3)	kT_{high} (keV) (4)	Abundance (solar) (5)	MEKAL Norm. ($\times 10^{-2}$) (6)	MKCFLOW \dot{M} ($M_{\odot} \text{ yr}^{-1}$) (7)	red. chi sq. (χ^2/dof) (8)
WABS \times MEKAL	1.5 ± 0.12	...	3.42 ± 0.02	0.43 ± 0.01	1.501 ± 0.009	...	745/735 = 1.014
WABS \times MEKAL	1.63 ± 0.19	...	3.39 ± 0.04	(0.4)	1.524 ± 0.008	...	754/736 = 1.025
WABS \times MEKAL	(2.48)	...	3.31 ± 0.03	(0.4)	1.55 ± 0.005	...	807/737 = 1.096
WABS \times [MEKAL + MEKAL]	(2.48)	2.68 ± 0.13	6.01 ± 1.05	(0.4)	$1.10 \& 4.57 \pm 2.06$...	759/735 = 1.032
WABS \times MKCFLOW	(2.48)	1.88 ± 0.07	5.33 ± 0.16	(0.4)	...	497 ± 33	763/736 = 1.04
WABS \times MKCFLOW	1.59 ± 0.17	1.87 ± 0.08	5.61 ± 0.17	(0.4)	...	454 ± 29	707/735 = 0.96
WABS \times [MEKAL + MKCFLOW]	(2.48)	(0.1)	3.47 ± 0.05	0.43 ± 0.018	1.47 ± 0.0002	22 ± 5	740/739 = 1.008

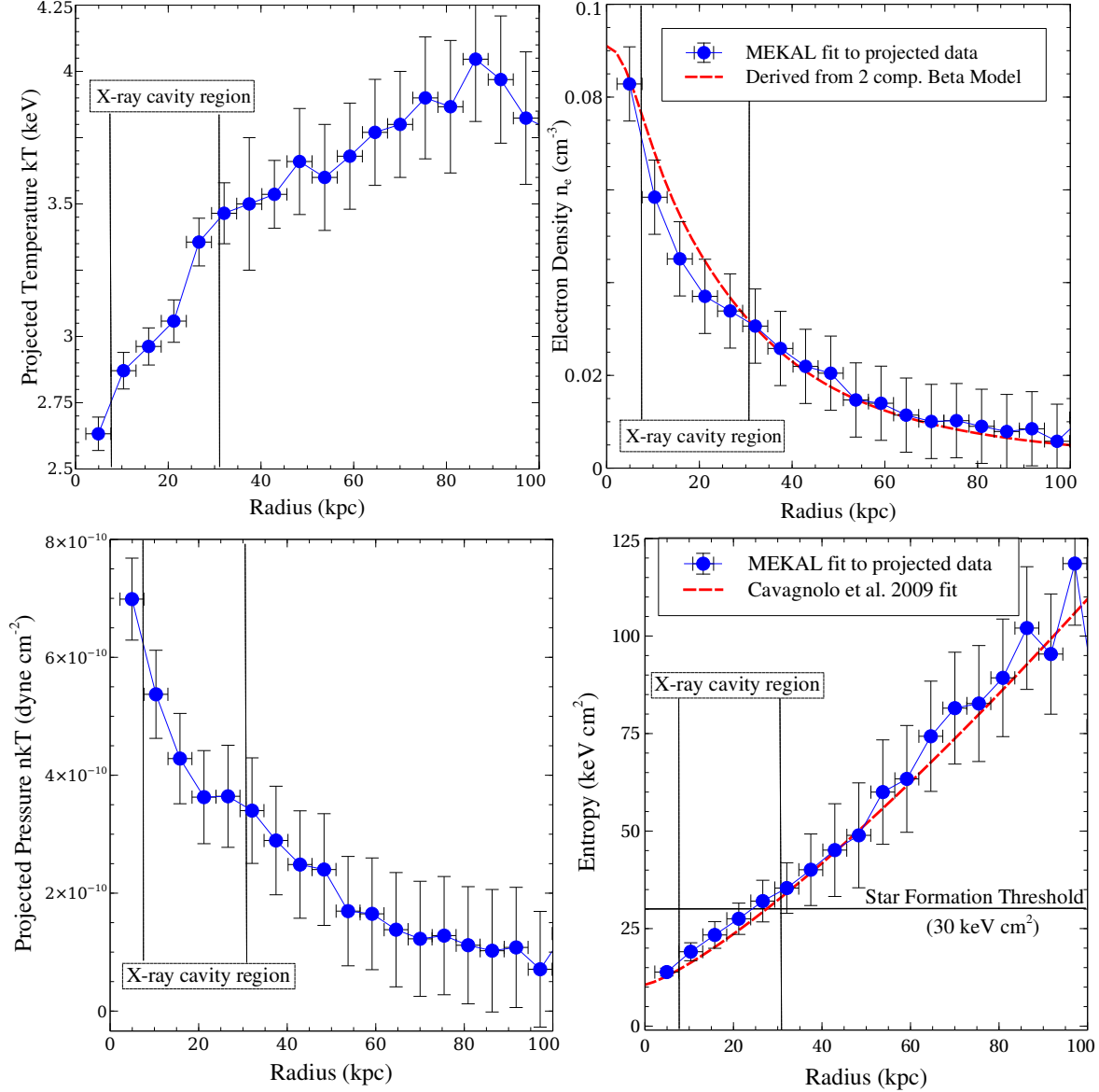


Figure 6. (*top left*) Projected temperature and (*top right*) projected density profiles derived from MEKAL thermal plasma models fit to radially extracted spectra from the inner 100 kpc of A2597. The temperature kT is a fit parameter from the MEKAL model. The electron density (n_e) was derived from the MEKAL normalization, while the pressure (P) and entropy (S) profiles, shown at (*bottom left*) and (*bottom right*), were calculated using $P = nkT$ (assuming $n = 2n_e$) and $S = kTn_e^{-2/3}$, respectively. In each profile we mark the ~ 25 kpc region permeated by the X-ray cavity network. Independent consistency checks on the electron density and entropy profiles are plotted in red. In the electron density plot, the consistency check is from the two-component additive beta model fit to the X-ray surface brightness profile. In the entropy profile, we plot the best-fit entropy profile from Cavagnolo et al. (2009).

previously mentioned 15 kpc NE filament becomes fainter at successively harder slices in energy space, and effectively disappears in the rightmost panel. The filament is therefore a relative soft excess, and is likely to be colder than the surrounding gas. The butterfly feature also loses much of its NE-SW width at higher energies while retaining effectively the same extension along the NW-SE axis that is aligned with the major axis of the BCG stellar isophotes. We have also created a hardness ratio map, but this will be discussed in the following section. In the 1-2 keV panel, we have marked the location of the “hot arc”, a feature which will be discussed in Sections 4 and 6.

We note that soft X-ray emission along lines of sight that pass through the galaxy midplane suffers more attenuation from the in-

trinsic hydrogen column than does hard X-ray emission. Moreover, as the line of sight moves away from the projected midplane, the absorbing hydrogen column gets smaller, resulting in smaller hardness ratios. It is therefore difficult to break the degeneracy between (a) true spatial distribution of soft vs. hard X-ray emitting gas and (b) preferred soft-end absorption by the BCG hydrogen column. By iteratively increasing the magnitude of the photoelectric absorption component in a `WABS×MEKAL` fit to the X-ray spectrum, we have estimated that a hydrogen column of $\gtrsim 10^{23}$ cm^{-2} would be required to attenuate enough of the soft X-ray flux to give rise to such confusion. Such a high column density is not consistent with results from our X-ray spectral modeling, as discussed in the sec-

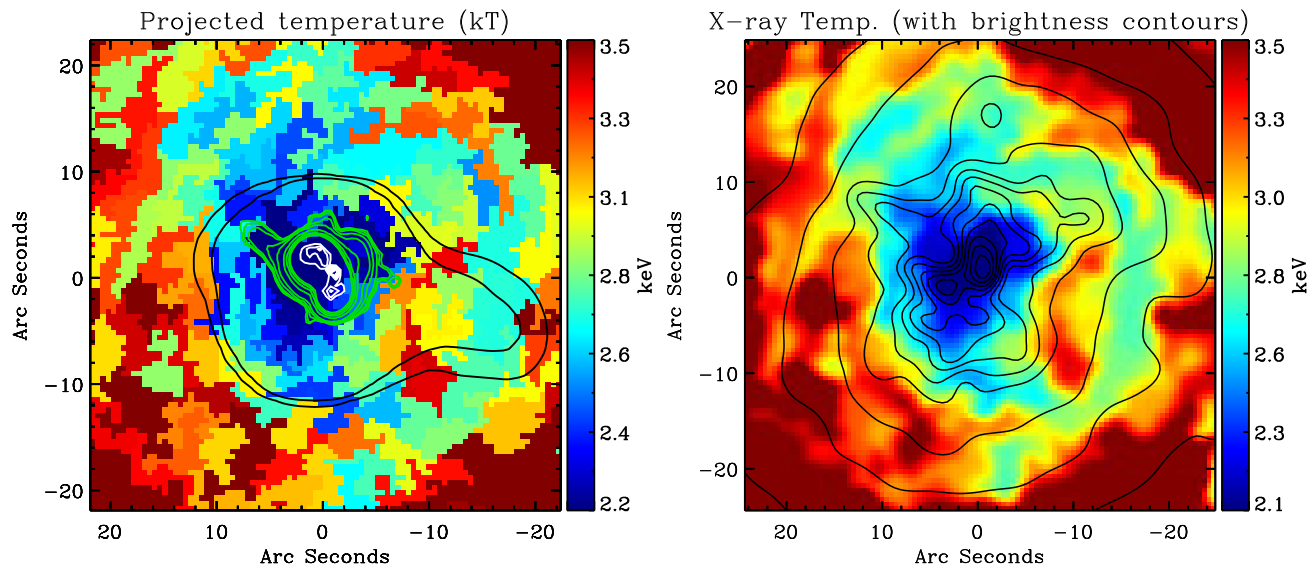


Figure 7. (*left*) X-ray temperature map created from spatially resolved *Chandra* spectroscopy of A2597. The best-fit single MEKAL model temperature is encoded via the scaled colorbar at the left of the figure. Note the $10''$ “cold filament” extending from the central cold (~ 2.2 keV) feature, as well as the “hot” arc-shaped feature $10''$ to the west. These features and their associated physical interpretations are discussed in the text. (*right*) Adaptively smoothed version of the same X-ray temperature map. X-ray surface brightness contours are overlaid in black. At the redshift of A2597, $1''$ corresponds to ~ 1.5 kpc. East is left, north is up.

tion above and shown in Table 1. We therefore consider it likely that the hard excess observed in the galaxy midplane is real.

3.6 Radial profiles of gas properties

We obtain radial profiles of temperature, density, pressure, and entropy by extracting spectra from both ObsIDs 7329 and 6934 using a series of 20 concentric circular annuli with a $1''.5$ inner radius, $3''.6$ stacking increment, and $74''$ outer radius. Weighted response matrices were generated, and the background-subtracted spectra from each annulus were fit simultaneously in XSPEC with absorbed MEKAL models (as before, N_H , Z , and z were frozen to the appropriate values). The extracted spectra are an emission-weighted superposition of properties along the line of sight extending through a 3D distribution of thermal plasma. Projection effects are therefore important, however typical “onion skin” spectral deprojection techniques are not appropriate in this case as the inner 100 kpc of X-ray emission shows very large departures from spherical symmetry. We therefore choose to show only projected spectral profiles².

In Fig. 6a through 6d we show the projected temperature, electron density, pressure, and entropy profiles (respectively) out to 100 kpc. The latter three quantities are derived from the MEKAL normalisation (emission measure) using the equations listed in the Fig. 6 caption, as well as a simple volume assumption. See Tremblay (2011) for more detail on how these profiles were obtained. We mark the location of the X-ray cavity network on each profile, and note a marginal steepening of the temperature gradient within this region. All of our profiles are consistent with past studies of both the early 18 ksec (good time) *Chandra* observation (ObsID 922, McNamara et al. 2001; Cavagnolo et al. 2009) as well as the

XMM-Newton observation of A2597 (Morris & Fabian 2005). We plot independent consistency checks on our density and entropy profiles by using our Beta model fit to the surface brightness profile and the entropy parametrization from Cavagnolo et al. (2009), respectively. The star formation threshold marked on the entropy profile is discussed in Tremblay et al. (2012b).

4 X-RAY SPECTRAL MAPS

In the left panel of Fig. 7 we present the projected X-ray temperature map. 330 MHz, 1.3 GHz, and 8.4 GHz radio contours are overlaid in black, green, and white, respectively. The right panel shows the same map, smoothed with an adaptive Gaussian kernel as a viewing aid. We overplot the adaptively smoothed X-ray surface brightness contours in black. The color map encodes the best-fit MEKAL gas temperature (kT) using the scale shown at the right of the figure. Both panels are aligned, and share the same ~ 60 kpc \times 60 kpc FOV centered on the X-ray centroid at RA=23h 25m 19.75s, Dec = $-12^\circ 07' 26.9''$ (J2000). East is left, north is up.

We first note that the overall temperature gradient is reasonably consistent with the projected radial temperature profile (Fig. 6a) over the same radius. We observe two significant spatial fluctuations from the azimuthally averaged temperature gradient, namely the “cold filament” and “hot arc” features, which are outlined and labeled accordingly in Fig. 8.

In comparing the top left panel with Fig. 2, it can be seen that the opening of the hot arc borders, in projection, the eastern edge of the western large cavity (features 1 and 2). The central axis of the extended western arm of the 330 MHz radio emission spatially coincides with the projected center of the hot arc structure, just as it does the western cavity.

As can be seen by comparing the temperature map with the overlaid X-ray surface brightness contours (right panel), the $10''$

² As a test, we did attempt spherical deprojection, and the results were very similar to our projected profiles.

(~ 15 kpc) cold filament is nearly cospatial with the bright X-ray filament seen in Fig. 1. In the hardness analysis presented in Section 3.5, we show that this bright filament is associated with an X-ray soft excess (see Fig. 4). There is slight spatial mismatch between the features, but this is not surprising given the spatial binning and smoothing processes undertaken during creation of the maps. Inevitably, this results in some loss of spatial information on at least the scale of the contour bin sizes. But when considered together, Figs. 4 and 7 clearly show that feature (5) in Fig. 2 is a “cold” filament.

In Fig. 9 we show the pseudo-entropy³, pseudo-pressure, metal abundance, and hardness ratio maps. We overlay 330 MHz and 1.3 GHz contours on the pseudo-entropy map (top left panel) in black and white, respectively. 330 MHz, 1.3 GHz, and 8.4 GHz contours are shown on the pseudo-pressure map (top right) in black, green, and white, respectively. We intentionally show fewer 330 MHz contours on the pseudo-entropy map to allow the hot arc feature to be clearly visible. On each map, the location of the hot arc feature seen in the X-ray temperature map is marked. Both pseudo-entropy and pseudo-pressure are elevated in the hot arc region. This result will be discussed in more detail in Section 6.

In the bottom left panel of Fig. 9 we show the metal abundance map. Kirkpatrick et al. (2011) studied metal abundance in A2597 in more detail than we will here. That work found higher abundance gas extended along the cavity and radio axis in A2597, and suggested that this could be evidence for a metal-enriched outflow driven by the radio source. Such a result is consistent with predictions from theoretical AGN feedback models (e.g., Pope et al. 2010; Gaspari et al. 2011), as well as results from other CC clusters (e.g. Hydra A, Simionescu et al. 2009; Gitti et al. 2011). Our abundance map has been made with large spatial bins using a S/N=70 threshold, as noted previously. This results in loss of spatial information on the scale of the cold filament and hot arc, though we do note that higher abundance gas is generally extended along the cavity and radio axis, consistent with the results from Kirkpatrick et al. (2011). Higher-than-average abundance is not observed at the location of the western large cavity (marked with the white arrow), but it is seen along its edges. This might be expected if the metal-enriched gas was pushed outward along the bubble boundary during the cavity excavation process.

In Fig. 9d we show an X-ray hardness ratio map, made by dividing the hard energy slice by the soft, then smoothing with a $1''.5$ Gaussian kernel (non-adaptive). The kernel size was chosen to roughly correspond with the spatial bin sizes used in the creation of the 2D spectral maps. The location of the hot arc corresponds to a region of relative hard excess that is roughly the same shape. Some mis-match in shape is expected, because the X-ray temperature map was created with the spatial contour binning process, and the hardness ratio map was not. As discussed in Section 3.5, there is always some degeneracy in this type of hardness analysis, as a region of hard excess can't necessarily be distinguished from a region of soft deficit or locally higher-than-average soft-end absorption by a more dense column of intervening hydrogen along the line of sight. In principle, the hot arc could merely be an artifact of this degeneracy, or a superposition of otherwise unrelated foreground features.

³ We use the term “pseudo” because the square root of the emission measure (i.e., the MEKAL normalization) is used as a proxy for the gas density. No inherently uncertain volume assumption is made, so this cannot be considered the actual gas density.

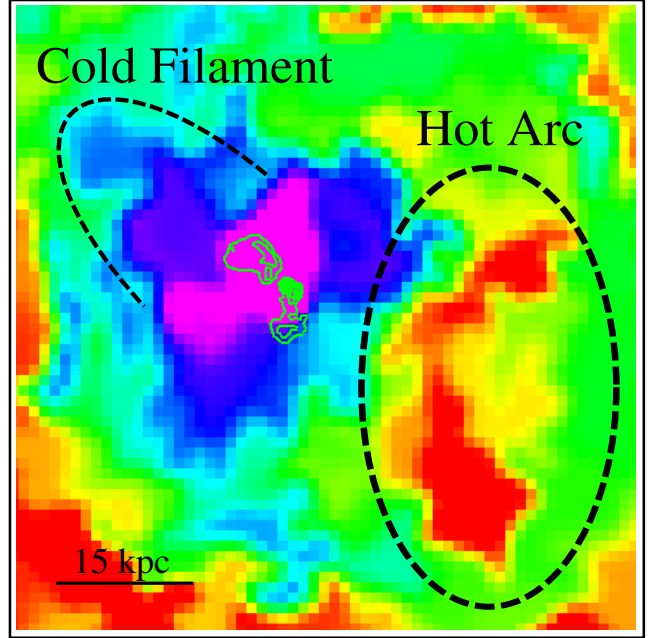


Figure 8. Zoom-in on the X-ray temperature map shown in Fig. 7. The central purple region of the map marks the location of the coolest ($\lesssim 2$ keV) X-ray gas. The cold filament and hot arc are labeled and outlined in black. Physical interpretations for these two features will be discussed in Sections 5 and 6.

We find these latter possibilities unlikely, simply because it's not clear why the soft X-ray extinction would be that patchy on such spatially small scales. It would also be a remarkable coincidence that a superposition of foreground features just happens to align in projection with the inner edge of the western X-ray cavity. In Section 6, we discuss how the hot arc may, given a large number of strong caveats, be a signature of ICM/ISM heating by the western large cavity as it buoyantly rises, dissipating its enthalpy as heat as ambient gas moves to refill its wake.

5 PHYSICAL INTERPRETATION OF THE COLD FILAMENT

As can be seen in Fig. 7, the 1.3 GHz radio emission (green contours) features a northeastern hook aligned along the same position angle as the cold filament. While the extended 1.3 GHz emission in this area covers only a small spatial fraction of the cold filament, it could be interpreted as evidence of dredge-up of low temperature, high density X-ray gas by the propagating radio source. Both the cold filament and the 1.3 GHz hook are aligned along the same position angle as the western large cavity, the extended 330 MHz emission, the projected VLBA jet axis, and the high velocity stream of warm optical line emitting gas observed in the Oonk et al. (2010) data. Although the 1.3 GHz hook is only cospatial with the bottom half of the cold filament, this should not necessarily be interpreted as the terminus of the jet. The 1.3 GHz data may simply not be sensitive enough to sample the regions of the jet beyond this location, or synchrotron losses could have rendered this part of the jet unobservable at these frequencies. The eastern extended “bump” of 330 MHz emission (black contours) suggests that radio structures lie beyond the maximal cluster-centric radius of the 1.3 GHz emission.

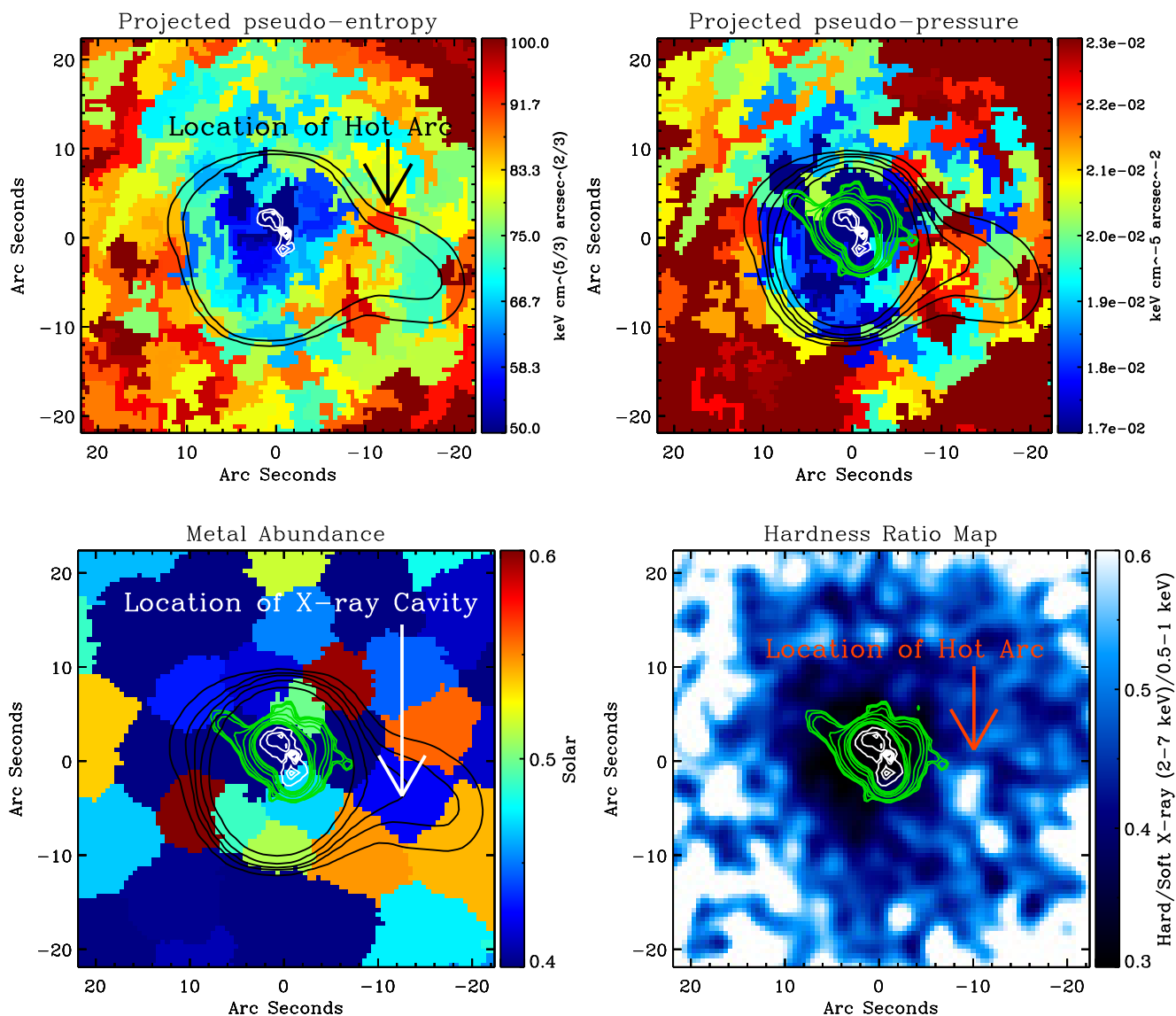


Figure 9. (*top left*) The same X-ray temperature map shown in Fig. 7, with 330 MHz, 1.3 GHz, and 8.4 GHz radio emission overlaid in black, green, and white contours, respectively; (*top right*) Pseudo-pressure map made by multiplying the temperature (kT) map at *left* with the square root of the emission measure map; (*bottom left*) metal abundance map, made with larger contour bins set by a $S/N=70$ threshold; (*bottom right*) X-ray hardness ratio map, made by dividing the exposure corrected 2-7 keV and 0.5-1 keV data. A gaussian kernel was used to smooth the hardness ratio map to roughly the same spatial resolution of the X-ray temperature and pressure maps. All panels share the same FOV, and are roughly 60 kpc on a side. The location of the hot arc (or large western cavity in the case of the abundance map) is marked with an arrow.

5.1 Possible theoretical models

We consider four possibilities for the cold filament.

(i) The cold filament could simply be the border between the neighboring cavities (features 3 and 4 Fig. 2).

(ii) The cold filament could be due to a morphologically complex multiphase cooling region around the bubbles.

(iii) Similar to scenario (ii), the filament could arise from displaced keV gas funneling (but not necessarily cooling) down the region separating the two neighboring X-ray cavities (features 3 and 4), or could arise from one larger cavity disrupting into two,

allowing for gas flow down what was formerly the center of the larger cavity.

(iv) The cold filament may be associated with dredge-up of multiphase gas by the propagating radio source and dragged outwards. The main evidence for this is that the filament is aligned along the same position angle as the projected jet axis, and partially cospatial with the extended 1.3 GHz hook. As we will discuss, there is additional multiwavelength evidence in support of this scenario.

We first note that our ability to discriminate between these scenarios is strongly limited by unknown projection effects. With this caveat in mind, we note that possibility (i), wherein the filament

Dredge-up of low entropy gas along jet propagation axis?

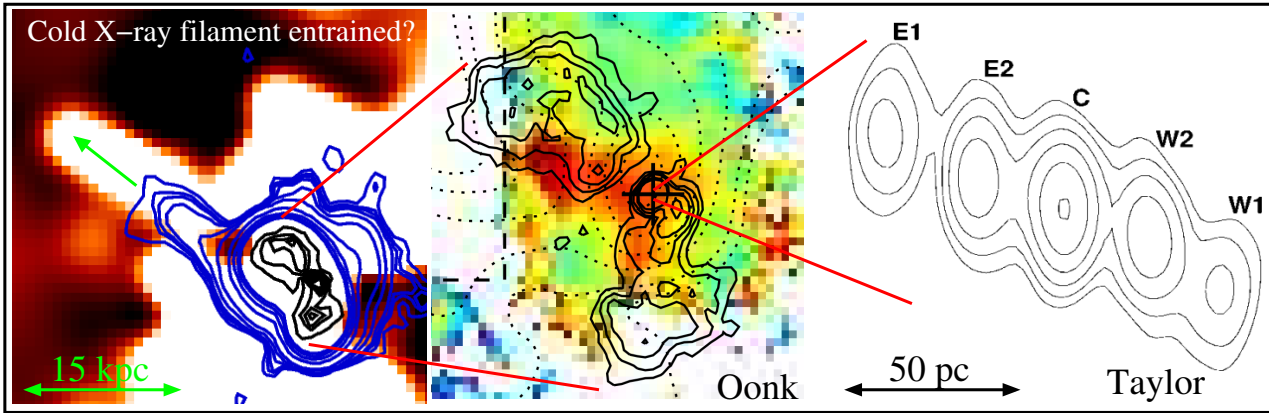


Figure 10. In the left panel, we show 8.4 GHz radio emission, in black, and 1.3 GHz radio emission, in blue, overlaid on the residual X-ray image from Fig. 2. The eastern edge of the 1.3 GHz emission is extended along the bottom half of the cold X-ray filament. The western edge of the 1.3 GHz emission is extended in the direction along the western large cavity, along with the 330 MHz extended emission, suggestive of a common axis offset from the central 8.4 GHz source. That the 1.3 GHz hook is cospatial with the soft excess X-ray filament may be consistent with a scenario wherein low entropy gas is dredged up by the propagating radio source (either during this epoch of activity or a previous one), as has recently been observed in Hydra A (Gitti et al. 2011). The center panel is a VLT SINFONI Paschen- α velocity dispersion map on the scale of the 8.4 GHz source, from Oonk et al. (2010). The higher velocity dispersion gas (in red) is aligned with the projected VLBA small scale jet axis, which we show in the right-most panel from Taylor et al. (1999). This could be evidence for entrainment of dense material by the propagating radio source. The FOV of the left-most panel is approximately $\sim 30 \text{ kpc} \times 30 \text{ kpc}$. The panels subsequently zoom in from there, to $10 \text{ kpc} \times 10 \text{ kpc}$ and $100 \text{ pc} \times 100 \text{ pc}$, respectively.

may simply be the border between two cavities, is the simplest and perhaps the most likely explanation as it relies on the least number of assumptions. This would not necessarily explain the observed soft excess associated with the filament.

Possibility (ii), wherein gas cools in a spatially complex manner around the cavities, is consistent with inhomogeneous cooling flow models generating thermally unstable filaments (e.g., Sharma et al. 2011; Fabian et al. 2011), and could explain the multiwavelength results discussed in Tremblay et al. (2012b). As discussed below, the cold filament is adjacent to (and not cospatial with) the optical emission line filaments shown in Fig. 6 of Tremblay et al. (2012b). This is contrary to simple expectations if the filament represents the hot phase of a multiphase cooling region that is forming the optical emission line filaments. Instead, the spatial relationship between the X-ray and optical filaments seems more consistent with scenarios in which the optical filaments have been swept aside by the 15 kpc X-ray filament, rather than formed from it.

Possibility (iii) is similarly difficult to interpret quantitatively, as projection effects make it impossible to know the real spatial relationship between the filament and its two apparently neighboring cavities. If two X-ray bubbles were buoyantly rising side-by-side, a large volume of the displaced ambient keV gas could be preferentially funneled into a column separating the two cavities. A larger bubble which has disrupted may result in a similar effect. Again, it is difficult to be more quantitative in considering these scenarios, for the reasons discussed above.

While much of this discussion is speculative, we note that possibility (iv) is supported by additional observational evidence. In this scenario, the cold filament may arise from dredge-up of lower temperature, higher density X-ray gas by the propagating radio source, as has recently been observed in the CC cluster Hydra A (Gitti et al. 2011). We provide a schematic for this scenario and some of this supporting evidence in Fig. 10. Comparing the left-most and rightmost panels of this figure, note the close projected position angle alignment between the cold filament and (1) the ex-

tended “hook” of the 1.3 GHz radio emission (blue contours) and (2) the projected current VLBA jet axis (Taylor et al. 1999). Note also that the filament is extended along the 330 MHz radio and X-ray cavity axis (see Fig. 2). Furthermore, the X-ray metal abundance map shown in Fig. 9c shows evidence for higher metallicity keV gas extended along this same axis, consistent with a picture in which enriched gas from the BCG nucleus has been dragged outwards.

Meanwhile, there have been prior suggestions that the “current” jet associated with the AGN may be entraining ambient warm and cold molecular gas. Oonk et al. (2010) presented *K*-band integral field (IFU) spectroscopy enabling gas kinematics analysis of the molecular and ionized gas distribution on the scale of the A2597 nebula and the 8.4 GHz radio source. They reported high velocity and velocity dispersion ($\sim 200 - 300 \text{ km s}^{-1}$) streams of H_2 and H II coincident with the southern edge of the northern 8.4 GHz radio lobe and approximately aligned with the VLBA jet axis. Another high velocity dispersion filament is coincident in projection with the eastern edge of the southern lobe. Their velocity dispersion map is shown in the center panel of Fig. 10. Oonk et al. (2010) considered two possible explanations for these high velocity dispersion features. If the radio source is a wide angle tail (WAT), the high velocity filaments may arise from the turbulent wake caused by relative motion of the AGN amid the ambient dense medium. This seems unlikely as the source is uncharacteristically compact relative to known WAT sources, and probably too small to be significantly affected by the host galaxy motion through the ICM.

Alternatively, the close projected alignment of the current VLBA jet axis for the northern lobe is suggestive of direct kinematical interaction (e.g., mass entrainment) between the jet and the gas through which it is propagating. In the latter case, the symmetry and asymmetry of the VLBA and 8.4 GHz counterjets, respectively, would require significant deflection of the current jet to account for the position angle mismatch between the 8.4 GHz lobes. A gradual bend in the jet owing to relative motion (consistent with the for-

mer scenario) may account for this. Interaction with the ambient medium may also produce a sharp trajectory deflection of a rapidly decelerating counterjet. The site of this possible deflection is not visible in the Onk et al. (2010) velocity maps, though the bright knot of 8.4 GHz radio emission immediately SW of the core may be related. Both scenarios are consistent with the steep lobe spectral index suggestive of dynamical frustration and confinement.

The bottom half of the cold filament is cospatial with extended 1.3 GHz radio emission (Fig. 10, blue contours). The width of this extended hook is approximately the width of the filament (~ 2 kpc), though it is slightly offset to the south from the filament’s major axis. Of course, the 1.3 GHz emission may not sample the entire jet, regardless of whether or not the filament was dragged upwards during this or a previous epoch of activity. The 1.3 GHz emission may sample only a small portion of the real jet, while the remainder of the emission may have aged to lower frequencies. The lower frequency 330 MHz emission is not resolved on these scales, so it is difficult to determine whether this may be the case, though it is worth noting that the 330 MHz emission does show a slight eastern extension at the same radius as the terminus of the cold filament, so some part of the jet (relic or otherwise) has made it out to these radii. Deeper radio data are needed to further study the apparent connection to the filament.

5.2 Energy arguments for the dredge-up model

As recently done in Gitti et al. (2011) for Hydra A, we can roughly estimate the energy that would be required to lift cold gas from the core to the projected height of the filament. To first order, this will be the difference in gravitational potential energy between the two locations. Assuming the local hot ISM is isothermal, hydrostatic, and with a sound speed $c_s \approx 750$ km s⁻¹ (Tremblay et al. 2012b), this will be

$$\Delta E = \frac{M_{\text{gas}} c_s^2}{\gamma} \ln \left(\frac{n_{e,i}}{n_{e,f}} \right). \quad (2)$$

where $\gamma \simeq 5/3$ is the ratio of specific heats. We roughly estimate the mass of the displaced X-ray gas (e.g., the mass of the cold filament), M_{gas} , by scaling inferred values for X-ray gas mass within ~ 100 kpc to a radius of 15 kpc, then scaling further to account for the filling factor of the cold filament. Allowing for a conservative range of inferred X-ray masses and filling factors, we estimate a cold filament mass range of $10^7 - 10^9 M_{\odot}$. The gas density at the bottom and top of the filament ($n_{e,i}$ and $n_{e,f}$, respectively) were estimated from the radial density profile (Fig. 6). We find the energy required to lift a $10^7 M_{\odot}$ filament out to 15 kpc to be 5.4×10^{56} ergs, while the energy required for a $10^9 M_{\odot}$ filament is on the order of 10^{58} ergs. These values are comparable to the pV energy of the X-ray cavities listed in Table 2 of Tremblay et al. (2012b), which can be considered rough lower limits on the AGN power output. If the AGN has been powerful enough in the past to expend $> 10^{56}$ ergs to excavate kpc-scale X-ray cavities, it is energetically feasible that it could also expend a similar amount of energy to entrain and lift cool X-ray gas out to 15 kpc.

6 PHYSICAL INTERPRETATIONS OF THE HOT ARC

We consider the following possibilities for the hot arc feature.

- (i) It could be an artifact of the process employed to make the

spectral maps and not associated with any real feature; or the spatial binning process could have exaggerated the significance and strength of a generally warmer but otherwise unremarkable region;

- (ii) The hot arc could be a superposition of real foreground features, or a localized region of soft X-ray *deficit* rather than a true hard X-ray *excess* that would be associated with truly hotter gas;

- (iii) The feature could be an artifact caused by a cool outer arc pushed out by the 330 MHz bubble;

- (iv) The hot arc could be a signature of the cavity heating process.

Concerning possibility (i): We have made numerous versions of the temperature map (for example, with various S/N binning thresholds and bin size ratio constraints) in an effort to explore the significance of the hot arc result. In the temperature map presented in this paper, there are ~ 14 (S/N=30, $\gtrsim 900$ count) bins that make up the hot arc feature, depending on how one defines its edges. Adjacent bins are fit with consistent temperatures that follow a steep gradient to the ambient colder temperature. The errors on the temperature fits to the spatial bins in the hot arc region are ± 0.25 keV. In test maps made with many small (S/N=10) bins, the feature persists. In maps made with very large round bins (e.g., S/N=70), the feature disappears, though this is not surprising. How the spectral extraction bins are tiled over the hot arc region has a strong effect on the apparent significance and shape of any such feature. A real sharp-edged localized spike in temperature could be smoothed out or “smudged” by bins which span both sides of the feature, resulting in temperature fits that reflect an average of the hotter gas and the ambient colder gas.

Concerning caveat (ii), we note that the feature does appear to be associated with an arc in the 1-2 keV panel of Fig. 4 (which we point out with an arrow), though its shape is somewhat dissimilar (this could simply be a consequence of smoothing). The hot arc is also associated with a hard excess arc in the hardness ratio map (Fig. 9d). Our X-ray observations are not deep enough, lacking the counts needed to determine whether the arc may be a site of higher intrinsic hydrogen column density that would lead to more soft X-ray absorption, especially considering the degenerate nature of X-ray spectral fitting. Given the strong spatial correspondence of the arc with the location and linear extent of the western cavity, the orientation of the 330 MHz radio source, VLBA jet, and 1.3 GHz emission, we find the latter possibility unlikely (because it would be a very big coincidence). For this same reason, we find it unlikely that the arc is a superposition of foreground features.

Assuming the hot arc is indeed a real feature, we speculate below on two possible physical interpretations (i.e., scenarios iii and iv).

6.1 Cool gas pushed outwards by the radio bubble?

The hot arc may be part of the general temperature gradient, but appear isolated because the 330 MHz radio bubble associated with the western large cavity has compressed and uplifted a rim of cooler gas from the center. Entrainment and displacement of colder ISM phases by ascending X-ray cavities has been observed before in other cool core clusters (e.g., recently in Perseus/NGC 1275, Fabian et al. 2011; and M87, Werner et al. 2010). Heightened metal abundance along the cavity/radio axis (see Fig. 9c) supports the possibility that the propagating radio source has displaced enriched colder gas from the core. The energy arguments for the cold X-ray filament discussed in Section 5 still apply here — the AGN is almost certainly powerful enough to uplift a significant gas mass out

ICM heated as it rushes to refill buoyant cavity wake?

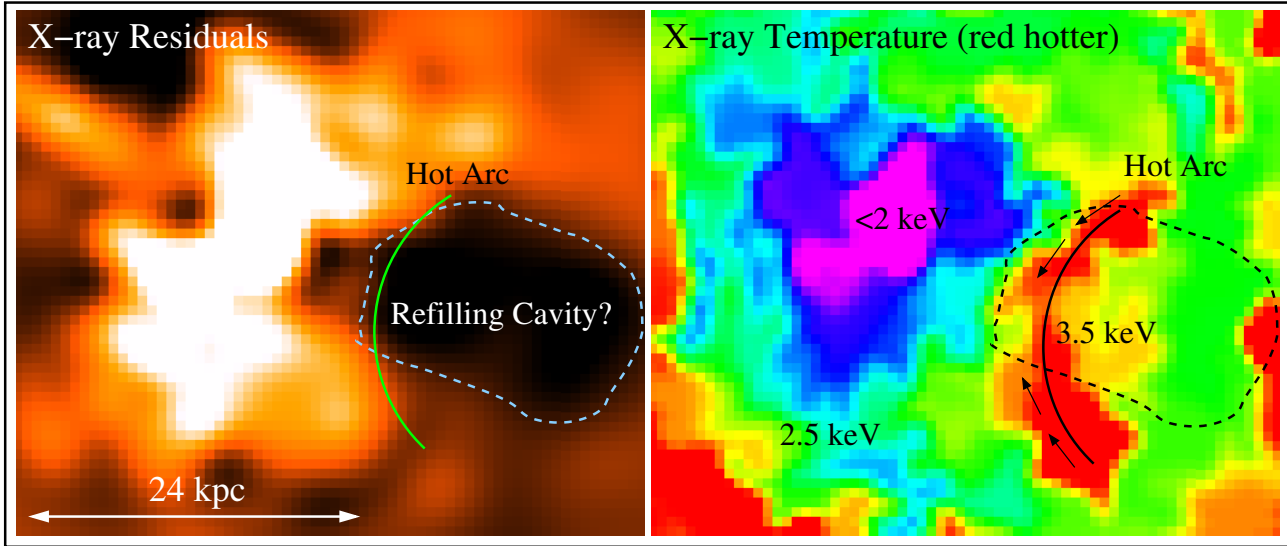


Figure 11. Zoom-in on (left) the residual X-ray image presented in Fig. 2 and (right) the temperature map to highlight the temperature features associated with the western large cavity, which we highlight with a dashed line in both figures. The FOV of both panels is identical. The green and black arcs traces the “hot arc” feature previously described in the temperature map. In the temperature map we draw arrows that illustrate our working interpretation for the “hot arc” feature. In this interpretation, the keV gas displaced by the buoyant rise of the M01 ghost cavity rushes inward to refill the resulting wake, thermalizing cavity enthalpy by heating the ambient gas > 1 keV above its ambient surroundings.

to a radius of ~ 20 kpc. The radio source at various frequencies exhibits evidence for complex dynamical interaction with optical and FUV filaments on ~ 10 kpc scales (e.g., Tremblay et al. 2012b). It seems reasonable that similar interactions could be occurring at ~ 20 kpc scales. The cooler region seen to the West of the hot arc ends at the projected terminus of the western large cavity. Beyond it, the spectral map shows hotter ~ 3.5 keV temperatures consistent with the local radial average. Uplifted cool gas is expected to have important consequences as it mixes with hotter gas at larger radii, such as lowering the net mass inflow rate and giving rise to efficient thermal conduction and ionizing interactions at the mixing interface (e.g., Werner et al. 2010).

6.2 A signature of cavity heating?

In Fig. 11 we provide a schematic for an alternative interpretation of the hot arc, assuming it is real. In simple AGN-driven cavity heating models, the enthalpy (free energy) of a buoyantly rising cavity can be entirely dissipated as the displaced thermal gas rushes to refill its wake (see e.g., the review by McNamara & Nulsen 2007). As the gas moves inward to fill the void left by the bubble, the corresponding change of gravitational potential energy is converted to kinetic energy, which then dissipates as heat. In principle, the kinetic energy created in the cavity wake is exactly equal to the enthalpy lost by the cavity during its corresponding ascent. Regardless of the Reynolds number of the plasma, viscous dissipation and turbulence ensures that kinetic energy of the infalling gas is damped rapidly, so thermalization occurs directly behind and on the same general scales as the bubble.

As seen in Fig. 11, the hot arc borders the inner edge of the western cavity, so its shape and location are consistent with the above scenario in which the gas in the arc has been heated during the buoyant passage of the bubble. We can make two simple

estimates to determine whether this makes sense in the context of available energy budgets. We first roughly estimate the total enthalpy H associated with the western cavity, which is the sum of the $p \times dV$ work associated with inflation and the thermal energy E of the cavity’s contents:

$$H = E + pV = \frac{\gamma}{\gamma - 1} pV, \quad (3)$$

where V is the cavity volume and p is the pressure of the radio lobe which displaced the thermal gas. Depending on its contents, cavity enthalpy is in the range of $2pV - 4pV$. Using this, we estimate the enthalpy associated with the western large cavity to be $\sim 7 \times 10^{58}$ erg, which is a rough limit on the energy reservoir that is (in principle) available to eventually heat the ICM over some unknown timescale (that is probably limited by the cavity lifetime).

As we did for the cold filament, we can use Equation 2 to estimate the change in gravitational potential energy associated with displacement of the hot arc gas. Using the same (very rough) estimation strategy as before, we assume that the mass of gas making up the hot arc is in the range of $10^7 - 10^9 M_{\odot}$ and that the density gradient and sound speed is the same as it was for the cold filament (the two features are roughly at similar radial distances). In this case, the gravitational potential energy change is between $10^{56} \lesssim \Delta E \lesssim 10^{58}$ ergs, of order what it was for the cold filament. If we assume this energy heats the gas, the corresponding temperature change can be simply approximated with $\Delta E = (3/2)Nk\Delta T$, where N is the number of particles. In estimating N , we use the electron density profile obtained in Section 3 and assume that the volume of the hot arc can be approximated by a spherical cap shape between 1%-30% the volume of the western large cavity. We find that, in principle, there is roughly enough energy to raise the local temperature of the hot arc by ~ 1 keV, which is what is observed in the temperature map.

Obviously, there are extremely uncertain assumptions behind

this estimate, so this is only useful as an order-of-magnitude consideration. In principle the hot arc would tap a fraction of the instantaneous cavity power P_{cav} of the western large cavity, or about $\sim 10^{42} - 10^{43}$ ergs s^{-1} (Tremblay et al. 2012b). The cooling luminosity associated with the inferred classical cooling flow is on the order of $3 \times 10^{43} \lesssim L_{\text{cool}} \lesssim 10^{44}$ ergs s^{-1} , so the hot arc could theoretically be associated with a significantly large fraction of ICM radiative losses. If real, this feature could be one of the first known observational signatures of the AGN cavity heating model invoked at late epochs to quench cooling flows (McNamara & Nulsen 2007).

If we assume that the arc is real and the interpretation is correct, then why is A2597 the only known cluster with a hot arc? There are numerous deep *Chandra* observations of X-ray cavities in CC clusters with published temperature maps (including maps with many more counts per square pc than ours), and no such feature has ever been reported before. Shocks and cold fronts can have similar morphologies as the hot arc, but our results are inconsistent in both orientation and spectral characteristics with these more commonly observed phenomenon. If the hot arc were a shock associated with the radio source, for example, we might expect the feature to be at the outer edge of the radio bubble with a concave-inward shape. There could be serendipity associated with detection of this feature. If we assume that all buoyantly rising X-ray cavities produce hot arcs in their wakes, their detectability would likely require (1) sufficiently deep X-ray observations; (2) X-ray spectral maps made with spatial bins that are individually smaller than the cavity; and (3) a large, $\gtrsim 10$ kpc cavity that is buoyantly rising in roughly the plane of the sky. The latter requirement seems necessary to recover the arc shape and concave-outward orientation. All of these detectability requirements are further dependent upon the unknown lifetime of such a temperature feature, especially if it is short lived. One possible explanation for why we do not see hot arcs associated with other cavities is that the locally heated gas mixes with the ambient colder gas or cools very quickly. The lifetime of an arc would strongly depend on the unknown role played by gas motions and/or thermal conduction.

7 SUMMARY

The primary results of this paper can be summarized as follows.

- New *Chandra* X-ray observations of Abell 2597 reveal a highly anisotropic surface brightness distribution, permeated by a network of X-ray cavities that is more extensive than previously known. The largest cavity is cospatial with extended 330 MHz radio emission.
- A ~ 15 kpc soft excess X-ray filament is found along the same position angle as the cavity/radio axis, and is partly cospatial with a hook of extended 1.3 GHz radio emission. Among several possible scenarios, we discuss multiwavelength evidence suggesting that the filament could be associated with the dredge-up of multiphase ($10^3 - 10^7$ K) gas by the propagating radio source. Although other interpretations are possible, we note that this model would be one of the most dramatic known examples of such an interaction.
- X-ray spectral maps reveal an arc of hot, high entropy gas bordering the inner edge of the largest X-ray cavity. We suggest that, if the feature is not an artifact, it could be due to (1) an uplifted rim of cold gas from the core, pushed outwards by the radio bubble; or (2) associated with cavity heating models invoked to quench cooling flows within the radio-mode AGN feedback interaction region.

Deeper radio data will be needed to study multiphase gas entrainment along the filament, and deeper X-ray data are needed to further understand the significance and implications of the hot arc.

ACKNOWLEDGMENTS

The authors thank Drs. Elaine Sadler, Robert Laing, Andy Robinson, Joel Kastner, and Bill Sparks for thoughtful discussions. We also thank the anonymous referee for constructive feedback. G. R. T. is grateful to R. A. S., and acknowledges support from the NASA/NY Space Grant Consortium, as well as a European Southern Observatory (ESO) Fellowship partially funded by the European Community's Seventh Framework Programme (FP7/2007-2013/) under grant agreement No. 229517. Partial support was provided by NASA through an award issued by JPL/Caltech, as well as the Radcliffe Institute for Advanced Study at Harvard University. T. E. C. was partially supported by NASA through *Chandra* award G06-7115B issued by the *Chandra* X-ray Observatory Center for and on behalf of NASA under contract NAS8-39073. Basic research into radio astronomy at the Naval Research Laboratory is supported by 6.1 Base funds. C. L. S. was supported in part by NASA *Herschel* Grants RSA 1373266, RSA P12-78175 and *Chandra* Grant G01-12169X. A. C. F. thanks the Royal Society. This paper is based upon observations with the *Chandra X-ray Observatory*, which is operated by the Smithsonian Astrophysical Observatory for and on behalf of NASA under contract NAS8-03060. We also make use of previously published observations by the NASA/ESA *Hubble Space Telescope*, obtained at the Space Telescope Science Institute, which is operated by the Association of Universities for Research in Astronomy, Inc., under NASA contract 5-26555. The National Radio Astronomy Observatory is a facility of the National Science Foundation operated under cooperative agreement by Associated Universities, Inc. We have made extensive use of the NASA Astrophysics Data System bibliographic services and the NASA/IPAC Extragalactic Database, operated by the Jet Propulsion Laboratory, California Institute of Technology, under contract with NASA.

REFERENCES

- Arnaud K. A., 1996, in *Astronomical Society of the Pacific Conference Series*, Vol. 101, *Astronomical Data Analysis Software and Systems V*, G. H. Jacoby & J. Barnes, ed., pp. 17–
 Batcheldor D., Tadhunter C., Holt J., Morganti R., O’Dea C. P., Axon D. J., Koekemoer A., 2007, *ApJ*, 661, 70
 Baum S. A., Heckman T. M., Bridle A., van Breugel W. J. M., Miley G. K., 1988, *ApJS*, 68, 643
 Birzan L., Rafferty D. A., McNamara B. R., Wise M. W., Nulsen P. E. J., 2004, *ApJ*, 607, 800
 Blanton E. L., Sarazin C. L., McNamara B. R., Wise M. W., 2001, *ApJ*, 558, L15
 Böhringer H., Voges W., Fabian A. C., Edge A. C., Neumann D. M., 1993, *MNRAS*, 264, L25
 Cavagnolo K. W., Donahue M., Voit G. M., Sun M., 2009, *ApJS*, 182, 12
 Churazov E., Brügggen M., Kaiser C. R., Böhringer H., Forman W., 2001, *ApJ*, 554, 261
 Clarke T. E., Sarazin C. L., Blanton E. L., Neumann D. M., Kasim N. E., 2005, *ApJ*, 625, 748
 De Young D. S., 1989, *ApJ*, 342, L59

- Elmegreen B. G., Elmegreen D. M., 1978, *ApJ*, 220, 1051
- Fabian A. C., 1994, *ARA&A*, 32, 277
- Fabian A. C., 2012, ArXiv e-prints
- Fabian A. C. et al., 2000, *MNRAS*, 318, L65
- Fabian A. C., Sanders J. S., Taylor G. B., Allen S. W., Crawford C. S., Johnstone R. M., Iwasawa K., 2006, *MNRAS*, 366, 417
- Fabian A. C., Sanders J. S., Williams R. J. R., Lazarian A., Ferland G. J., Johnstone R. M., 2011, ArXiv e-prints
- Fanaroff B. L., Riley J. M., 1974, *MNRAS*, 167, 31P
- Forman W. et al., 2007, *ApJ*, 665, 1057
- Forman W. et al., 2005, *ApJ*, 635, 894
- Fruscione A. et al., 2006, in Presented at the Society of Photo-Optical Instrumentation Engineers (SPIE) Conference, Vol. 6270, Society of Photo-Optical Instrumentation Engineers (SPIE) Conference Series
- Gaspari M., Ruszkowski M., Sharma P., 2011, ArXiv e-prints
- Gitti M., Nulsen P. E. J., David L. P., McNamara B. R., Wise M. W., 2011, *ApJ*, 732, 13
- Holt J., Tadhunter C. N., Morganti R., 2008, *MNRAS*, 387, 639
- Holt J., Tadhunter C. N., Morganti R., Emonts B. H. C., 2011, *MNRAS*, 410, 1527
- Kirkpatrick C. C., McNamara B. R., Cavagnolo K. W., 2011, *ApJ*, 731, L23
- Koekemoer A. M., O’Dea C. P., Sarazin C. L., McNamara B. R., Donahue M., Voit G. M., Baum S. A., Gallimore J. F., 1999, *ApJ*, 525, 621
- McNamara B. R., Nulsen P. E. J., 2007, *ARA&A*, 45, 117
- McNamara B. R., Nulsen P. E. J., 2012, ArXiv e-prints
- McNamara B. R., O’Connell R. W., 1993, *AJ*, 105, 417
- McNamara B. R. et al., 2000, *ApJ*, 534, L135
- McNamara B. R. et al., 2001, *ApJ*, 562, L149
- Morris R. G., Fabian A. C., 2005, *MNRAS*, 358, 585
- Nulsen P. E. J., McNamara B. R., Wise M. W., David L. P., 2005, *ApJ*, 628, 629
- O’Dea C. P., Baum S. A., 1986, Radio continuum processes in clusters of galaxies; Proceedings of the Workshop, Green Bank, WV, Aug. 4-8, 1986 (A88-38551 15-90). Charlottesville, VA, National Radio Astronomy Observatory, 1986, p. 141-146., 16, 141
- O’Dea C. P., Baum S. A., Mack J., Koekemoer A. M., Laor A., 2004, *ApJ*, 612, 131
- Oonk J. B. R., Jaffe W., Bremer M. N., van Weeren R. J., 2010, *MNRAS*, 405, 898
- Peterson J. R., Fabian A. C., 2006, *Phys. Rep.*, 427, 1
- Pope E. C. D., Babul A., Pavlovski G., Bower R. G., Dotter A., 2010, *MNRAS*, 406, 2023
- Rafferty D. A., McNamara B. R., Nulsen P. E. J., Wise M. W., 2006, *ApJ*, 652, 216
- Russell H. R., Fabian A. C., Sanders J. S., Johnstone R. M., Blundell K. M., Brandt W. N., Crawford C. S., 2010, *MNRAS*, 402, 1561
- Sanders J. S., 2006, *MNRAS*, 371, 829
- Sarazin C. L., 1986, *Reviews of Modern Physics*, 58, 1
- Sarazin C. L., Burns J. O., Roettiger K., McNamara B. R., 1995, *ApJ*, 447, 559
- Sharma P., McCourt M., Quataert E., Parrish I. J., 2011, ArXiv e-prints
- Simionescu A., Werner N., Böhringer H., Kaastra J. S., Finoguenov A., Brüggén M., Nulsen P. E. J., 2009, *A&A*, 493, 409
- Taylor G. B., O’Dea C. P., Peck A. B., Koekemoer A. M., 1999, *ApJ*, 512, L27
- Tremblay G., 2011, PhD thesis, RIT
- Tremblay G. R. et al., 2012b, *MNRAS* in press
- Voit G. M., 1988, *ApJ*, 331, 343
- Werner N. et al., 2010, *MNRAS*, 407, 2063